Zhang *et al. Energy Mater* 2024;4:400043
DOI: 10.20517/energymater.2023.102

Energy Materials

Article

Open Access

Check for updates

Modulation of physical and chemical connections between SiO_x and carbon for high-performance lithium-ion batteries

Kaiyuan Zhang[1], Jiarui Xing[1], Huili Peng[1], Jichao Gao[1], Shuheng Ai[1], Qiwang Zhou[1], Di Yang[1,*], Xin Gu[2,*]

[1]School of Chemistry and Chemical Engineering, Linyi University, Linyi 276005, Shandong, China.
[2]College of New Energy, State Key Laboratory of Heavy Oil Processing, China University of Petroleum (East China), Qingdao 266580, Sahndong, China.

[*]**Correspondence to:** Dr. Di Yang, School of Chemistry and Chemical Engineering, Linyi University, the west side of the north section of Industrial Avenue, Lanshan District, Linyi 276005, Shandong, China. E-mail: yangdi@lyu.edu.cn; Prof. Xin Gu, College of New Energy, State Key Laboratory of Heavy Oil Processing, China University of Petroleum (East China), 66 Changjiang West Road, Huangdao District, Qingdao 266580, Shandong, China. E-mail: guxin@upc.edu.cn

How to cite this article: Zhang K, Xing J, Peng H, Gao J, Ai S, Zhou Q, Yang D, Gu X. Modulation of physical and chemical connections between SiO_x and carbon for high-performance lithium-ion batteries. *Energy Mater* 2024;4:400043. https://dx.doi.org/10.20517/energymater.2023.102

Received: 11 Dec 2023 **First Decision:** 29 Feb 2024 **Revised:** 5 Apr 2024 **Accepted:** 30 Apr 2024 **Published:** 14 May 2024

Academic Editors: Cheol-Min Park, Meicheng Li **Copy Editor:** Dong-Li Li **Production Editor:** Dong-Li Li

Abstract

SiO_x is an encouraging anode material for high-energy lithium-ion batteries owing to the following unique characteristics: a relatively high theoretical capacity, low operating potential, ample resource availability, and, most importantly, lower volume changes compared to Si. However, its utilization has been hindered by a significant ~200% volume change during lithiation and low conductivity, leading to the breakdown of anode materials and accelerated capacity degradation. This study presents a novel SiO_x/G/C composite comprising SiO_x nanoparticles, graphite, and carbon nanotubes fabricated through a simple ball milling and annealing process. This composite features a dual-carbon framework interconnected with SiO_x via C–O–Si bonds, enhancing reaction kinetics and accommodating volume fluctuations. These enhancements translate into remarkable advancements in cycling stability and rate performance. Specifically, as-prepared SiO_x/G/C exhibits a high capacity retention of ~700 $mAh·g^{-1}$ over 500 charging/discharging times at 1.0 $A·g^{-1}$. Furthermore, when incorporated into a full-cell configuration (SiO_x/G/C//$LiNi_{1/3}Co_{1/3}Mn_{1/3}O_2$), this system demonstrates a reversible capacity of 113 $mAh·g^{-1}$ over 100 cycles at 1.0 $mA·cm^{-2}$, underscoring its practical viability.

Keywords: SiO_x anode, lithium-ion batteries, silicon-carbon composite, dual-carbon engineering, chemical binding

INTRODUCTION

Lithium-ion batteries (LIBs) have become ubiquitous in portable electronic equipment, electric vehicles, and smart grids[1-3]. However, the slow advancement in their energy density poses a challenge to meeting the demands of rapidly evolving energy storage applications. It is imperative to focus on developing advanced anode materials to tackle this challenge, especially if enhancing existing cathode materials proves difficult[4,5]. The SiO_x ($0 < x < 2$) anode has several advantages. First, SiO_x has a high theoretical specific capacity, such as ~1,900 $mAh \cdot g^{-1}$ for SiO_2 and ~2,700 $mAh \cdot g^{-1}$ for SiO, facilitating the realization of high-energy-density LIBs[6,7]. Second, it is abundant and can be readily prepared on a large scale from agricultural waste[8]. Lastly, SiO_x-based anodes generate Li_2O and Li silicate during cycling, ensuring greater cycling stability than Si-based anode materials[9-10]. However, SiO_x experiences a volumetric change of 200% during lithiation, leading to anode material breakdown and rapid capacity deterioration[11,12]. Furthermore, it exhibits low conductivity, approximately 6.7×10^{-4} $S \cdot cm^{-1}$, leading to poor rate capability. SiO_x-carbon composites have been proposed to mitigate these significant challenges. These composites demonstrate promising electrochemical performance, leveraging the superior electronic conductivity and superior mechanical properties of carbon materials[13-15].

Carbon nanotubes (CNTs) are highly conductive and remarkably elastic. They are widely used to address SiO_x-related challenges[16]. However, given their one-dimensional (1D) nature, CNTs often require support from other carbon materials when paired with SiO_x. Alternatively, two-dimensional (2D) graphene or three-dimensional (3D) graphite are viable alternatives[17,18]. For example, SiO_x-graphite composites have been recognized as encouraging candidates for high-performance LIBs, benefiting from enhanced capacity and conductivity of graphite. Nevertheless, the unique alloying-intercalation mechanism inherent in SiO_x-graphite anodes presents significant obstacles, including volume fluctuations and an unstable solid-electrolyte interface. Graphene, derived from graphite, is an excellent support material for high-performance SiO_x anodes in LIBs because it can mitigate volume changes, shorten lithium-ion transmission pathways, and increase conductivity[19]. However, differences in morphology between 0D SiO_x particles and 1D CNTs or 3D graphite/2D graphene pose challenges in achieving robust interface adhesion between SiO_x and carbon. The weak interfacial interaction forces between SiO_x and carbon impede effective interfacial electron transfer and structural stability within the carbon network. A potential solution is to establish chemical bonds with active materials, thereby fostering a cohesive structure that enhances the high specific capacity of SiO_x while preventing their displacement[20]. Addressing this challenge entails creating a 3D carbon network through chemical bonding, incorporating multiple carbon dimensions. However, identifying a preparation strategy that is both scalable and highly efficient for this approach remains challenging[21].

This study introduces a conductive dual-carbon network consisting of 1D CNTs and 3D graphite, chemically bonded with SiO_x via C–O–Si linkages, facilitated by high-energy ball milling. This network was devised to enhance the electrochemical capabilities of 0D SiO_x nanoparticles. The synergistic effect of CNTs and graphite was shown through control groups wherein SiO_x was mixed solely with CNTs (SiO_x/C) or graphite (SiO_x/G). Fourier transform infrared spectroscopy (FTIR) analyses confirmed the formation of C–O–Si bonds, which agreed well with those results in X-ray photoelectron spectroscopy (XPS), validating their role in improving the electrochemical properties of SiO_x/G/C electrodes. The dual-carbon network enveloped SiO_x, reducing volume fluctuations and establishing efficient pathways for lithium transport. Consequently, SiO_x supported by this dual-carbon interaction (SiO_x/G/C) exhibited enhanced cycling performances and superior rate capability.

EXPERIMENTAL

Preparation of SiO_x/G/C, SiO_x/G, and SiO_x/C

The materials used in the experiment were SiO (99.99% metal basis) from Aladdin, graphite (AR) from Macklin, and CNTs from Aladdin. They were used as is, without any further purification. The experiment involved adding 0.3 g of micro SiO, 60 mg of graphite, and 60 mg of CNTs to a 50 mL agate jar containing 10 g of agate balls, which was performed in the Ar-filled glove box. The jar was then sealed and transferred to a ball milling machine. The mixture was milled for 24 h at the rotation speed of 600 $r \cdot min^{-1}$. After milling, the mixed product was annealed for 3 h at 900 °C in an Ar atmosphere and cooled naturally to create the SiO_x/G/C composite. To compare, the control groups of SiO_x/C and SiO_x/G were prepared using the same process as SiO_x/G/C but without introducing CNTs and graphite, respectively.

Material characterization

The field-emission scanning electron microscope from Germany, the Zeiss Gemini 300 type, was used to get scanning electron microscopy (SEM) photos, while a JEOL JEM 1011 transmission electron microscope from Japan records transmission electron microscopy (TEM) images for this work. A JEOL JEM F200 transmission electron microscope from Japan records the High-resolution TEM (HRTEM) images. XPS results and X-ray diffraction (XRD) data were collected from a Thermo Fischer ESCALAB 250 X-ray photoelectron spectrometer (from the USA) and a Bruker D8 Advance X-ray diffractometer (from Germany), respectively. In addition, Raman spectra and FTIR results were obtained from HORIBA JYHR800 and Bruker Tensor 27 spectrometers from Japan and Germany, respectively. Thermal gravimetric analysis (TGA) was collected by a Mettler Toledo TGA/SDTA851 thermal gravimetric analyzer from Switzerland.

Electrochemical measurements

A SiO_x/G/C electrode, a lithium metal counter electrode, and a separator (Celgard 2400 type) were assembled into coin cells (CR2032 type) in an argon-filled glovebox to fabricate half cells. On a Cu-foil current collector, a slurry was coated, comprising as-prepared SiO_x/G/C (70 wt%), conductive carbon black (20 wt%), and cellulose sodium (10 wt%) dispersed in deionized (DI) water. After drying and punching, we obtained 1.2 cm wafers of the SiO_x/G/C electrode with an average mass loading of 1.2 $mg \cdot cm^{-2}$. To assemble full cells, a prelithiated SiO_x/G/C anode, $LiNi_{1/3}Co_{1/3}Mn_{1/3}O_2$ (NCM111) cathode, and Celgard 2400 separator were combined into CR2032 coin cells within an argon-filled glovebox. A nickel cobalt manganese (NCM) cathode was prepared by pasting a slurry onto an Al foil. The N-methyl pyrrolidone was used to mix the slurry, which contained commercial $LiNi_{0.3}Co_{0.3}Mn_{0.3}O_2$ (80 wt%), conductive carbon black (20 wt%), and polyvinylidene fluoride (10 wt%). Both half and full cells used 1.0 $mol \cdot L^{-1}$ $LiPF_6$ in ethylene carbonate/dimethyl carbonate (volume ratio, 1:1) with 7% fluoroethylene carbonate. We conducted galvanostatic charging/discharging tests on both the half (0.01-1.5 V) and full cells worked at 2.8-4.2 V, using a battery testing system (LAND CT2001A). Additionally, electrochemical impedance spectroscopy (EIS) of SiO_x/G/C half cells was tested with a frequency range of 100 kHz to 0.01 Hz, and their cyclic voltammetry (CV) test was working at a scan rate of 0.1-1.0 $mV \cdot s^{-1}$.

RESULTS AND DISCUSSION

The preparation process of the SiO_x/G/C composite, depicted in Figure 1A, involves ball milling and annealing. First, SiO, graphite, and CNTs were combined in a ball milling jar and sealed in an argon-filled glovebox to prevent further oxidation of SiO. Through high-energy ball milling, the raw materials were uniformly mixed and reduced by adjusting the number of agate balls with different sizes. Subsequently, the annealing phase, conducted under an argon atmosphere at 900 °C, induced the disproportion reaction, yielding the SiO_x/G/C product. TEM and SEM photos of the SiO_x/G/C composite (presented in Figure 1B and C, respectively) confirm the uniform wrapping of SiO_x nanoparticles within a network of conductive

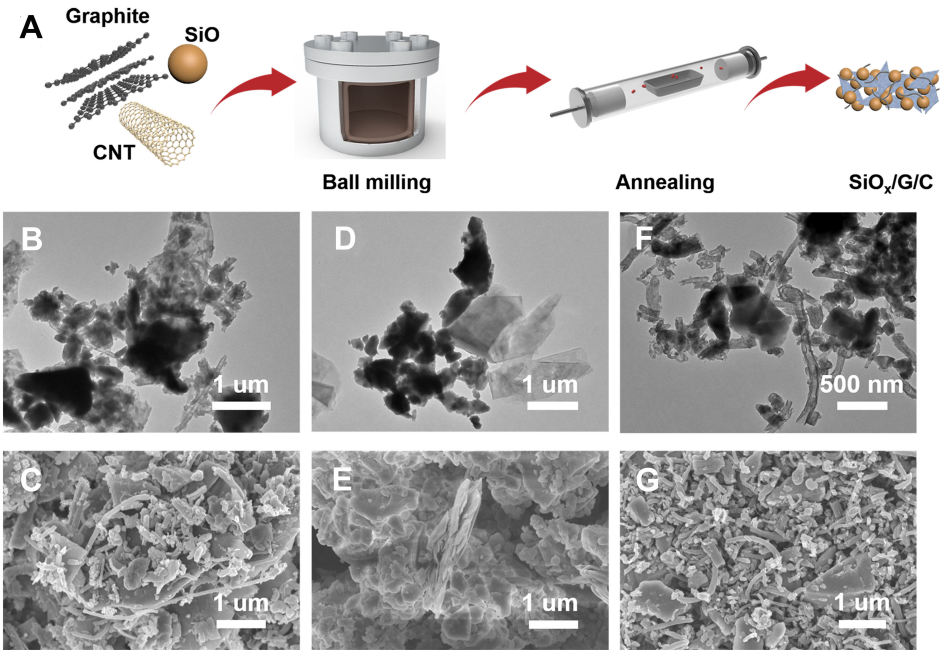

Figure 1. (A) Preparation strategy of SiO_x/G/C composite; (B) TEM image and (C) SEM image of SiO_x/G/C; (D) TEM photo and (E) SEM photo of SiO_x/G composite; (F) TEM image and (G) SEM imageof SiO_x/C composite. CNT: Carbon nanotube; TEM: transmission electron microscopy; SEM: scanning electron microscopy.

carbon. Energy dispersive X-ray spectroscopy mapping shown in Supplementary Figure 1 reveals the uniformity of the SiO_x/G/C composite. This close contact between SiO_x and the dual-carbon network buffers volume changes during cycling and enhances electron transport pathways for the SiO_x/G/C. HRTEM images of SiO_x/G/C in Supplementary Figure 2A confirm the crystalline structure of CNTs and graphite [Supplementary Figure 2B] and the amorphous structure of SiO_x [Supplementary Figure 2C]. Furthermore, SiO_x particle sizes, determined to be less than 500 nm, confirm the efficiency of the ball milling method. The lattice fringes of graphite in SiO_x/G/C, corresponding to (002) planes, were calculated to be approximately 0.33 nm. However, the TEM image of SiO_x/G [Figure 1D] illustrates inadequate attachment of SiO_x particles to graphite sheets, even after sonication, indicating the potential for CNTs to assist in exfoliating graphite. Additionally, SEM images of SiO_x/G [Figure 1E] confirm that graphite alone is insufficient for rapidly forming a carbon network and embedding SiO_x. The TEM [Figure 1F] and SEM images [Figure 1G] of the SiO_x/C composite demonstrate efficacy of CNTs in preventing SiO_x nanoparticle aggregation. However, owing to their 1D morphology, SiO_x particles in the SiO_x/C composite are more exposed than those in the SiO_x/G/C sample. From the abovementioned results, creating a robust framework to stabilize SiO_x with just one type of carbon material is challenging. However, leveraging the advantages of 3D graphite and 1D CNTs makes uniform dispersion of SiO_x within a dual-carbon network achievable. This approach ensures structural stability and prevents electrical contact loss during cycling.

To examine the structure and components of the SiO_x/G/C, SiO_x/G, and SiO_x/C composites, different techniques, including XRD, Raman, FTIR spectroscopy, and XPS, were employed. XRD analysis [Figure 2A] elucidated the structural characteristics of the three composites mentioned earlier. Peaks observed at 26.6°, 44.6°, 54.7°, and 77.5° were identified as the diffraction planes of (002), (101), (004), and (110) for graphite (JCPDS no. 04-0836)[22], respectively. The characteristic graphite peak at 26.6° observed in SiO_x/G also appeared in SiO_x/G/C. Peaks at 26.4° and 44.7° (SiO_x/C) relatively weaker than graphite in SiO_x/G/C and SiO_x/G composites corresponded to the (003) and (101) diffraction planes, indicating the presence of

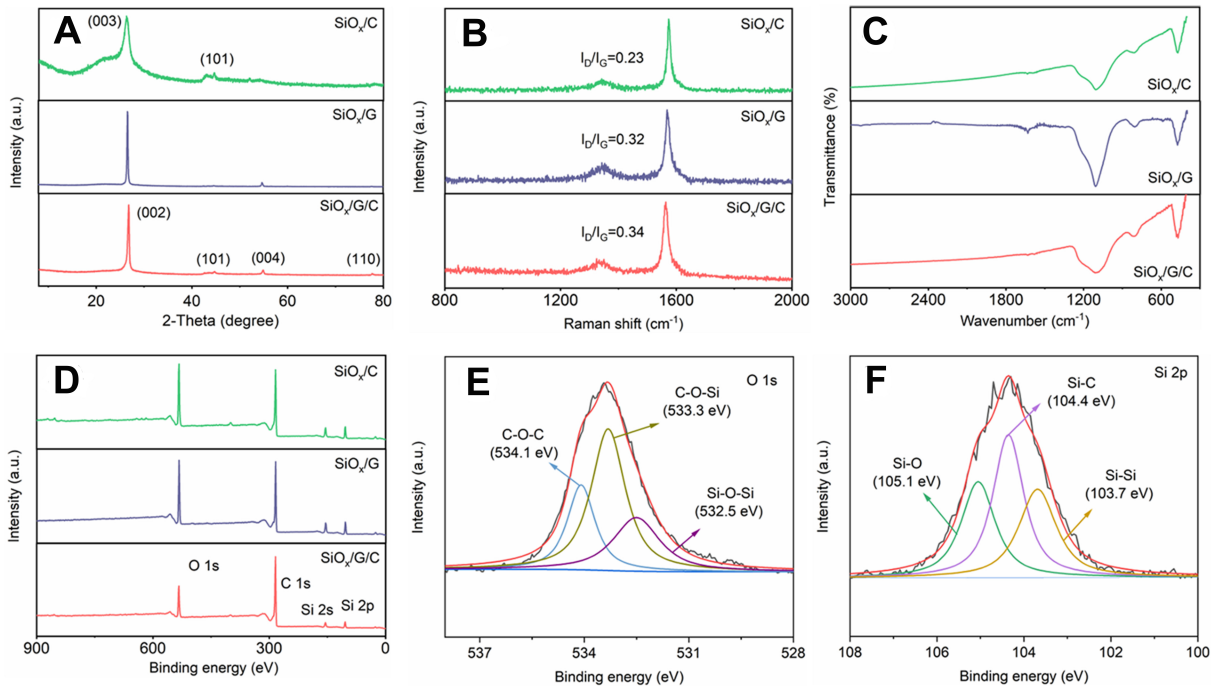

Figure 2. (A) XRD results, (B) Raman and (C) FTIR spectrum of SiO_x/G/C, SiO_x/G and SiO_x/C composites; (D) XPS spectrum of SiO_x/G/C, SiO_x/G, and SiO_x/C; SiO_x/G/C's XPS spectrum of (E) O 1s and (F) Si 2p. XRD: X-ray diffraction; FTIR: Fourier transform infrared spectroscopy; XPS: X-ray photoelectron spectroscopy.

CNTs[23,24]. Additionally, a broad diffraction peak around 22.3° was indexed to the amorphous SiO_x[25] in SiO_x/C. Raman spectra shown in Supplementary Figure 3 confirmed the low crystallinity SiO_x with a broad peak at 459 cm^{-1}[26], consistent with XRD data. The presence of carbonaceous materials in the three previously mentioned samples was confirmed by D and G bands at approximately 1,324 and 1,564 cm^{-1}, respectively, [Figure 2B]. The intensity ratio of the D-and G-Raman peaks (I_D/I_G value) of SiO_x/G/C composites of 0.34 suggested a high degree of graphitization, beneficial for the performances of SiO_x-carbon anodes[27,28]. The FTIR spectrum [Figure 2C] exhibited two peaks in SiO_x/G/C at 1,630 and 1,677 cm^{-1}, corresponding to the C=O and C=C bonds, similar to those peaks observed in SiO_x/C and SiO_x/G, indicative of sp^2 carbon hybridization[29]. Peaks located at 1,103, 808, and 470 cm^{-1} were attributed to bending and asymmetric stretching vibrations of SiO_x[30]. Comparison of FTIR spectra between SiO_x nanoparticles (derived from ball milling micro SiO) and SiO_x/G/C [Supplementary Figure 4] confirmed the formation of C–O–Si bonds. The disappearance of the broad peak located at 3,435 cm^{-1}, assigned to the vibration of the –OH bond in SiO_x, in SiO_x/G/C suggests that the -OH of SiO_x might combine with the dual-carbon network to form C–O–Si covalent bonds. Si–O–Si bonds in SiO_x and SiO_x/G/C are located at 1,086 and 1,103 cm^{-1}, respectively. The shift in these two peaks is attributed to the C–O–Si bond formation at 1,230 cm^{-1} in SiO_x/G/C, consistent with previous reports[31]. XPS spectra of SiO_x/G/C, SiO_x/G, and SiO_x/C are depicted in Figure 2D, with similar peaks around 533, 284, 155, and 104 cm^{-1} assigned to O 1s, C 1s, Si 2s, and Si 2p, respectively. Further insights into electronic structure of the SiO_x/G/C composite were obtained from the O 1s, Si 2p, and C 1s XPS spectra, as shown in Figures 2E and F, and Supplementary Figure 5, respectively. The O 1s spectrum in Figure 2E contains three peaks corresponding to C–O–Si, C–O–C, and Si–O–Si bonds[32], confirming the effect of ball milling in promoting the formation of a C–O–Si bond in the SiO_x/G/C. The Si 2p spectrum [Figure 2F] exhibits three peaks: Si–O (105.1 eV), Si–C (104.4 eV), and Si–Si (103.7 eV)[33]. Analysis of the C 1s spectrum [Supplementary Figure 5] reveals peaks at 285.1, 284.2, and 283.8 eV, attributed to C=O, C–O, and C–C/C=C bonds, respectively[34]. These findings confirm the creation

of a chemical bond between SiO_x and carbon, enhancing charge transfer and increasing structural stability. To accurately determine the relative ratios of SiO_x in the SiO_x/G/C composite, TGA results (SiO_x/G/C) were conducted [Supplementary Figure 6], revealing a SiO_x content of 72%.

The lithium storage performance of three types of anodes, namely SiO_x/G/C, SiO_x/G, and SiO_x/C, was investigated to assess their efficacy of a dual-carbon network for SiO_x. Figure 3A reveals CV curves of the SiO_x/G/C anode for the initial five cycles, elucidating the charging and discharging reactions. The cathodic peaks observed at 0.01 and 0.17 V indicate alloy reactions between Li and Si, while the anodic peaks at 0.51, 0.18, and 0.33 V were attributed to the de-alloying of Li_xSi. The increasing CV area from the first to the fourth cycle suggests an activation process during cycling. Conversely, the remarkable similarity between the fourth and fifth curves implies the potential stability of the SiO_x/G/C over several cycles[35,36].

Figure 3B illustrated voltage curves of the SiO_x/G/C anode about the first three charging/discharging cycles in the range from 0.01 to 1.5 V at a smaller current density of 0.1 $A \cdot g^{-1}$. It delivers high initial discharging/charging capacities of 2,617/1,674 $mAh \cdot g^{-1}$, respectively, delivering an unsatisfactory initial coulombic efficiency (ICE) of 64%. The phenomenon is attributed to irreversible formation of Li_2O and lithium silicates, which could potentially be addressed by prelithiation technology[37].

Discharging capacities of SiO_x/G/C acquired by changing current densities are presented in Figure 3C and D, showcasing its superior rate capabilities compared to SiO_x/C and SiO_x/G. The discharging capacity of SiO_x/G/C was 1,482 $mAh \cdot g^{-1}$ when working at a current density of 0.5 $A \cdot g^{-1}$. While at 6.0 $A \cdot g^{-1}$, it maintains a better capacity (347 $mAh \cdot g^{-1}$), surpassing those common results of SiO_x/G and SiO_x/C when performed at equivalent current densities. Remarkably, after 100 cycles of comparison, with the current density reverting to 1.0 $A \cdot g^{-1}$, the discharge capacity of SiO_x/G/C recovers to 855 $mAh \cdot g^{-1}$, indicating satisfactory rate capability. The initial ICE was verified through the voltage variations of SiO_x/G and SiO_x/C (Supplementary Figures 7 and 8, respectively) at 0.1 $A \cdot g^{-1}$ for the first charging or discharging time. Consequently, SiO_x/G and SiO_x/C demonstrated ICE values of 62.0% and 64.9%, respectively, indicating minimal changes in ICE despite the construction of the carbon network. Superior performance of the SiO_x/G/C anode is attributed to reinforced electronic/ionic conductivity and surface passivation facilitated by the dual-carbon network.

Figure 3E depicts the cycling performance of three electrode types: SiO_x/G/C, SiO_x/G, and SiO_x/C. Notably, SiO_x/G/C outperforms control groups at 1.5 $A \cdot g^{-1}$, sustaining an encouraging capacity of 675 $mAh \cdot g^{-1}$ over 300 cycles. This highlights the pivotal role of the dual-carbon network in enhancing the Li^+ storage performance of SiO_x/G/C as an anodic material compared to control groups. Moreover, a high areal capacity of the SiO_x/G/C electrode, acquired at 2.0 $mA \cdot cm^{-2}$, of 1.67 $mAh \cdot cm^{-2}$ exhibits consistent capacity retention over 100 cycles, even loaded about 2.2 $mg \cdot cm^{-2}$ [Figure 3F], underscoring its promising potential for practical application. Long-term cycling performance of SiO_x/G/C [Figure 3G] was demonstrated. Following activation (0.2 $A \cdot g^{-1}$) in the initial three cycles, SiO_x/G/C underwent cycling at 1.0 $A \cdot g^{-1}$ for 500 cycles, delivering a noteworthy lithium storage of approximately 700 $mAh \cdot g^{-1}$ with a capacity retention of 78% (compared to the fourth cycle, 898 $mAh \cdot g^{-1}$). This performance surpasses that of many recently reported SiO_x-based anodes for LIBs [Supplementary Table 1][18,21,25,38-43].

The electrical resistivities of SiO_x/G/C, SiO_x/C, and SiO_x/G samples were analyzed to discern differences in the conductive mechanism [Figure 4A]. The detailed electrical resistivity data of SiO_x/G/C are provided in Supplementary Table 2. Results indicated that SiO_x/C and SiO_x/G exhibited higher electrical resistivities of 0.129 and 0.151 Ω·cm, respectively, compared to 0.075 Ω·cm for SiO_x/G/C. Enhanced electrical conductivity of SiO_x/G/C can be attributed to as-prepared dual-carbon network, facilitating a higher electron transfer

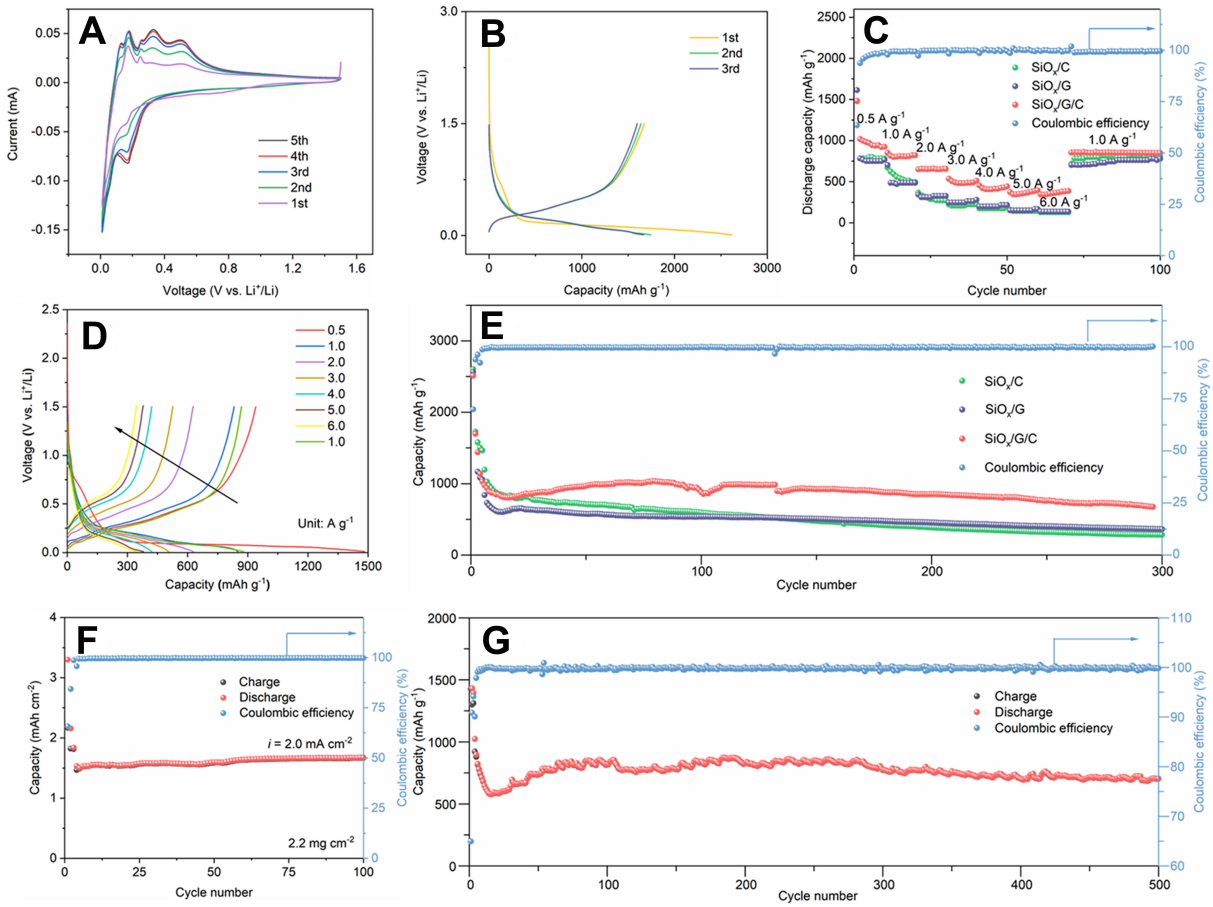

Figure 3. (A) CV curves and (B) voltage curves results of the SiO_x/G/C electrode; (C) Rate capabilities of SiO_x/G/C electrodes at different current densities compared with control groups; (D) SiO_x/G/C's charging and discharging voltage curves under different current densities; (E) SiO_x/G/C's cyclic capabilities at 1.5 $A{\cdot}g^{-1}$ compared with control groups; (F) Thick SiO_x/G/C (~2.2 $mg{\cdot}cm^{-2}$) electrode's cycling performance at 2.0 $mA{\cdot}cm^{-2}$; (G) SiO_x/G/C's long-term cycling performance of electrode at 1.0 $A{\cdot}g^{-1}$. CV: Cyclic voltammetry.

rate. Figure 4B shows the electrochemical mechanism of SiO_x/G/C through CV data at varied scan rates ranging from 0.1 $mV{\cdot}s^{-1}$ to 1.0 $mV{\cdot}s^{-1}$. Notably, anodic (peak A) and cathodic peaks (peaks B and C) exhibit similar profiles as the sweep rates increase, indicating favorable reaction kinetics and minimal electrode polarization. Further insights into the diffusion-controlled and capacitive-controlled mechanisms of the SiO_x/G/C anode were obtained by analyzing the relationship between peak current (i) and scan rate (v), denoted as[44]:

$$i = av^b \tag{1}$$

$$\log i = b \log v + \log a \tag{2}$$

After analyzing and fitting the data for peaks A, B, and C, the b-values for each peak are illustrated in Figure 4C. Peak B exhibits a b-value of 0.48, closely approaching 0.5, indicative of a diffusion-controlled process. Conversely, peaks A and C have estimated b-values of 0.85 and 0.63, respectively, suggesting a mixed storage mechanism with a dominance of the capacitive mechanism. This hybrid mechanism combines the high capacity of SiO_x with the cyclic stability of the dual-carbon network, resulting in

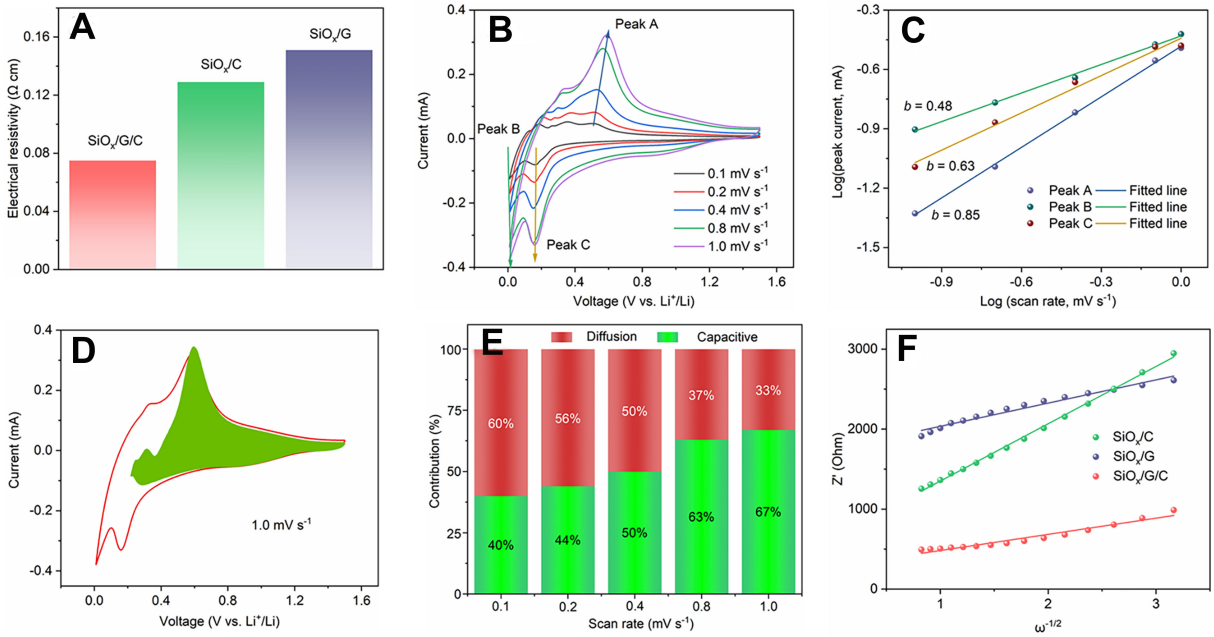

Figure 4. (A) Electrical resistivities of the SiO_x/G/C and other two samples; (B) CV data of the SiO_x/G/C at changing scan rates; (C) Fitted lines and corresponding *b*-value resulted from the value of log(*i*, peak current) *vs.* log(*v*, scan rate) for SiO_x/G/C electrode; (D) Contribution of capacitive charge storage to the total capacity of SiO_x/G/C at a higher scan rate (1.0 $mV \cdot s^{-1}$); (E) Two kinds of charge storage distribution ratios with the same scan rates; (F) The relationships of Z′ and $\omega^{-1/2}$ for the SiO_x/G/C and the other two control groups. CV: Cyclic voltammetry.

satisfactory performance. Furthermore, the ratio of the capacitive contribution in the hybrid mechanism was determined by[45]:

$$i = k_1 v + k_2 v^{1/2} \tag{3}$$

After calculating the values of k_1 and k_2, we confirmed the capacitive- and diffusion-controlled ratios. For instance, at scan rates of 1.0 and 0.1 $mV \cdot s^{-1}$, 67% and 40% of the capacitive-controlled ratios were calculated, respectively [Figures 4D and Supplementary Figure 9]. Furthermore, the capacitive-controlled ratio [Figure 4E] was determined under the same scan rates as those in Figure 4B, revealing an increasing proportion of capacitive contribution with increasing scan rates, which is advantageous for high-rate charging or discharging. The enhanced reaction kinetics of SiO_x/G/C compared with the control groups was investigated using the EIS test [Supplementary Figure 10]. Detailed parameters of EIS [Supplementary Table 3] and the equivalent circuit [Supplementary Figure 11] were analyzed and fitted, with the SiO_x/G/C anode exhibiting lower resistance than the control groups. This can be attributed to the unique dual-carbon network comprising graphite and CNTs. Furthermore, the lithium-ion diffusion coefficient for SiO_x/G/C and the control groups was calculated by[33]:

$$D_{Li^+} = 0.5\left(\frac{RT}{AF^2\sigma C}\right)^2 \tag{4}$$

Where *R* (gas constant), *F* (Faraday constant) and *T* (absolute temperature) remain constant. Surface area of the electrode, labeled as *A*, could result from the as-prepared electrode, and molar concentration of Li^+,

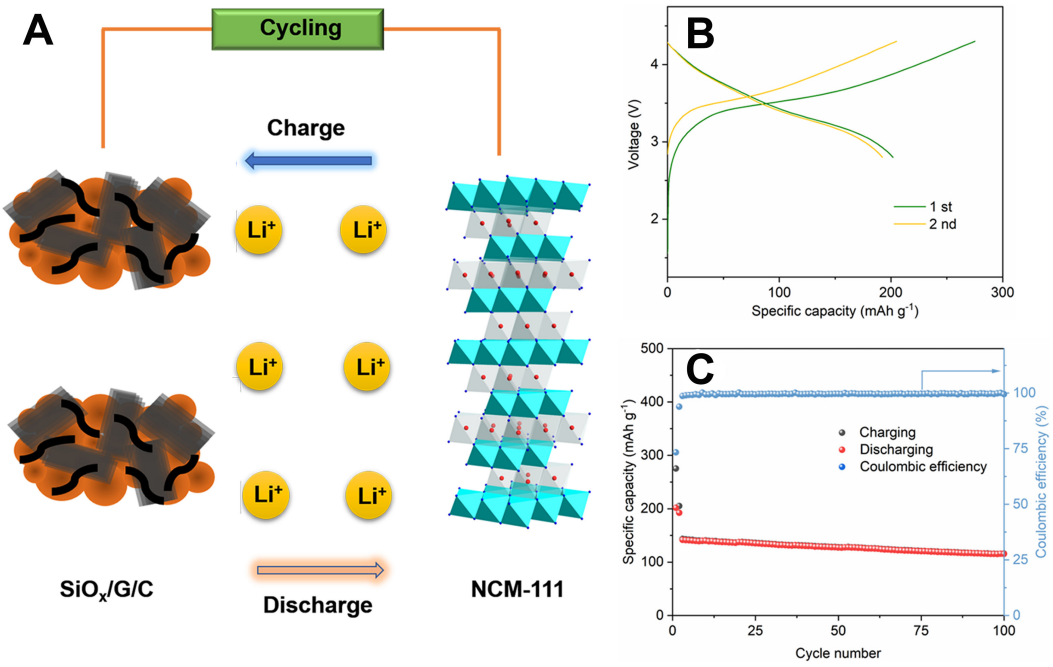

Figure 5. (A) Design of the SiO_x/G/C//NCM111 full cell; (B) Charging/discharging voltage profiles; (C) Cyclic performances of SiO_x/G/C//NCM111 full cell at 1.0 mA·cm^{-2}.

named *C* in Equation (4), could be calculated by the electrolyte, with the σ-value determining the D_{Li^+} for SiO_x/G/C and other two electrodes. By establishing the connection between *Z'* and $\omega^{-1/2}$ in low-frequency part of EIS, the σ-values could be fitted and correlated to the slopes of the lines in Figure 4F, calculated using[33]:

$$Z' = R_D + R_L + \sigma\omega^{-1/2} \quad (5)$$

The minimum σ-value observed for SiO_x/G/C indicates the superior Li^+ diffusion coefficient, aligning well with the cyclic performance and rate capability demonstrated in Figure 3.

To assess the application potential of the SiO_x/G/C, it is paired with a NCM111 cathode [Figure 5A]. In the first step, SiO_x/G/C was combined with lithium foil and cycled multiple times until the coulombic efficiency (CE) of the half-cell reached 99%. This step aimed to minimize initial lithium loss in full cells. Subsequently, the delithiated SiO_x/G/C anode was paired with the NCM111 cathode, and the setup was cycled at 0.2 mA·cm^{-2} for the first two cycles, followed by 1.0 mA·cm^{-2} for subsequent cycles. The voltage curves of a SiO_x/G/C//NCM111 full cell during charging and discharging at 2.8-4.2 V are depicted in Figure 5B. The cell exhibits initial charging/discharging capacities of 275.2 and 201.8 mAh·g^{-1}, respectively, delivering an ICE of 73%. Its cyclic performance is presented in Figure 5C, demonstrating satisfactory lithium storage of 116 mAh·g^{-1} over 100 cycles. These results underscore the exceptional performance of SiO_x/G/C in full cells.

CONCLUSIONS

In summary, to address the challenges of high volume variation and slow reaction dynamics associated with SiO_x anodes, we devised a dual-carbon network utilizing 3D graphite and 1D CNTs through a straightforward and highly effective ball milling and annealing process. This novel dual-carbon network,

possessing strong electrical connections to SiO_x nanoparticles via C–O–Si bonds, mitigated the volume variation of SiO_x and facilitated smooth Li^+ transport, ensuring the retention of high capacity advantages of SiO_x-based anodes. Leveraging the benefits of this chemically bound dual-carbon network, both Li//SiO_x/G/C half cells and SiO_x/G/C//NCM111 full cells demonstrated remarkable performance, delivering an encouraging lithium storage of ~700 mAh·g^{-1} over 500 cycles and 116 mAh·g^{-1} for 100 cycles. These results underscore the considerable potential of our approach, offering both scalable preparation and performance enhancement for high-energy storage materials.

DECLARATIONS

Authors' contributions

Conceptualization, methodology, investigation, writing - original draft: Zhang K
Formal analysis, investigation, data curation: Xing J
Formal analysis: Peng H
Resources: Gao J
Investigation, data curation: Ai S
Visualization: Zhou Q
Resources, supervision: Yang D
Methodology, supervision, writing - review and draft: Gu X

Availability of data and materials

The datasets generated or analyzed during this study are available from the corresponding authors upon reasonable request.

Financial support and sponsorship

The authors thank the Natural Science Foundation of Shandong Province (Nos. ZR2022QB182, ZR2022MB088) and the National Natural Science Foundation of China (No. 22378426).

Conflicts of interest

All authors declared that there are no conflicts of interest.

Ethical approval and consent to participate

Not applicable.

Consent for publication

Not applicable.

REFERENCES

1. Wang D, Ma Y, Xu W, et al. Controlled isotropic canalization of microsized silicon, enabling stable high-rate and high-loading lithium storage. *Adv Mater* 2023;35:e2212157. DOI PubMed
2. Cao Z, Zheng, X, Qu Q, Huang Y, Zheng H. Electrolyte design enables a high-safety and high-performance Si anode with a tailored electrode-electrolyte interphase. *Adv Mater* 2021;33:e2103178. DOI PubMed
3. Gu X, Wang J, Zhao X, et al. Engineered nitrogen doping on VO_2(B) enables fast and reversible zinc-ion storage capability for aqueous zinc-ion batteries. *J Energy Chem* 2023;85:30-8. DOI
4. Liu Z, Yu Q, Zhao Y, et al. Silicon oxides: a promising family of anode materials for lithium-ion batteries. *Chem Soc Rev* 2019;48:285-309. DOI
5. Fan X, Wang C. High-volatge liquid electrolytes for Li batteries: progress and perspectives. *Chem Soc Rev* 2021;50:10486-566. DOI
6. Luo H, Zhang X, Wang Z, et al. Self-lithiation electrode with improved lithium-ion transport kinetics enables fast-charging SiO_x-based

anode for lithium-ion batteries. *Chem Eng J* 2023;469:143677. DOI

7. Xu Q, Sun JK, Yu ZL, et al. SiO_x encapsulated in graphene bubble film: an ultrastable Li-ion battery anode. *Adv Mater* 2018;30:e1707430. DOI PubMed
8. Padwal C, Pham HD, Hoang LTM, Mundree S, Dubal D. Deep eutectic solvents assisted biomass pre-treatment to derive sustainable anode materials for lithium-ion batteries. *Sustain Mater Techno* 2023;35:e00547. DOI
9. Zhou X, Liu Y, Ren Y, et al. Engineering molecular polymerization for template-free SiO*x*/C hollow spheres as ultrastable anodes in lithium-ion batteries. *Adv Funct Mater* 2021;31:2101145. DOI
10. Liu Z, Zhao Y, He R, et al. Yolk@shell SiO*x*/C microspheres with semi-graphitic carbon coating on the exterior and interior surfaces for durable lithium storage. *Energy Storage Mater* 2019;19:299-305. DOI
11. Guo C, Xie Y, Pan K, Li L. MOF-derived hollow SiO*x* nanoparticles wrapped in 3D porous nitrogen-doped graphene aerogel and their superior performance as the anode for lithium-ion batteries. *Nanoscale* 2020;12:13017-27. DOI
12. Chen L, Zheng J, Lin S, et al. Synthesis of SiO*x*/C composite nanosheets as high-rate and stable anode materials for lithium-ion batteries. *ACS Appl Energy Mater* 2020;3:3562-8. DOI
13. Qiu J, Guo J, Li J, et al. Insight into the contribution of the electrolyte additive $LiBF_4$ in high-voltage $LiCoO_2$||SiO/C pouch cells. *ACS Appl Mater Interfaces* 2023;15:56918-29. DOI PubMed
14. Zhang Z, Zhang Y, Ye M, Tang Y, Liu X, Li CC. An in situ constructed Li^+-conductive interphase enables high-capacity and high-rate SiO_x/C anode. *J Power Sources* 2022;542:231795. DOI
15. Wang H, Que X, Liu Y, et al. Facile synthesis of yolk-shell structured SiO_x/C@Void@C nanospheres as anode for lithium-ion batteries. *J Alloy Compd* 2021;874:159913. DOI
16. Guo W, Yan X, Hou F, et al. Flexible and free-standing SiO_x/CNT composite films for high capacity and durable lithium ion batteries. *Carbon* 2019;152:888-97. DOI
17. Zhang Y, Wang WP, Zhao Y, et al. Exacerbated high-temperature calendar aging of SiO*x*-graphite electrode induced by interparticle lithium crosstalk. *Adv Funct Mater* 2023;34:2310309. DOI
18. Sun M, Xu Z, Liu K, et al. Construction of rice husk-derived SiO_x nanoparticles encapsulated with graphene aerogel hybrid for high-performance lithium ion batteries. *Electrochim Acta* 2022;422:140572. DOI
19. Son Y, Kim N, Lee Y, et al. Calendering-compatible macroporous architecture for silicon-graphite composite toward high-energy lithium-ion batteries. *Adv Mater* 2020;32:2003286. DOI
20. Liu S, Zhang X, Yan P, et al. Dual bond enhanced multidimensional constructed composite silicon anode for high-performance lithium ion batteries. *ACS Nano* 2019;13:8854-64. DOI PubMed
21. Fang T, Liu H, Luo X, et al. Accommodation of two-dimensional SiO*x* in a point-to-plane conductive network composed of graphene and nitrogen-doped carbon for robust lithium storage. *ACS Appl Mater Interfaces* 2022;14:53658-66. DOI PubMed
22. Zhang K, Du W, Qian Z, et al. SiO_x embedded in N-doped carbon nanoslices: a scalable synthesis of high-performance anode material for lithium-ion batteries. *Carbon* 2021;178:202-10. DOI
23. Xue H, Cheng Y, Gu Q, et al. An SiO*x* anode strengthened by the self-catalytic growth of carbon nanotubes. *Nanoscale* 2021;13:3808-16. DOI
24. Tian H, Tian H, Yang W, et al. Stable hollow-structured silicon suboxide-based anodes toward high-performance lithium-ion batteries. *Adv Funct Mater* 2021;31:2101796. DOI
25. Xie H, Hou C, Qu Y, et al. N-SiO*x*/graphite/rGO-CNTs@C composite with dense structure for high performance lithium-ion battery anode. *J Energy Storage* 2023;72:108452. DOI
26. Xu Q, Sun JK, Yin YX, Guo YG. Facile synthesis of blocky SiO*x*/C with graphite-like structure for high-performance lithium-ion battery anodes. *Adv Funct Mater* 2018;28:1705235. DOI
27. Lu C, Li X, Liu R, et al. Optimized Ti-O subcompounds and elastic expanded MXene interlayers boost quick sodium storage performance. *Adv Funct Mater* 2023;33:2215228. DOI
28. Zhang K, Mao H, Gu X, Song C, Yang J, Qian Y. ZIF-derived cobalt-containing N-doped carbon-coated SiO*x* nanoparticles for superior lithium storage. *ACS Appl Mater Interfaces* 2020;12:7206-11. DOI PubMed
29. Hasan MT, Gonzalez-Rodriguez R, Ryan C, Faerber N, Coffer JL, Naumov AV. Photo-and electroluminescence from nitrogen-doped and nitrogen-sulfur codoped graphene quantum dots. *Adv Funct Mater* 2018;28:1804337. DOI
30. Zhang K, Zhao D, Qian Z, Gu X, Yang J, Qian Y. N-doped Ti_3C_2T*x* MXene sheet-coated SiO*x* to boost lithium storage for lithium-ion batteries. *Sci China Mater* 2023;66:51-60. DOI
31. Xu E, Zhang Y, Lin L. Improvement of mechanical, hydrophobicity, and thermal properties of chinese fir wood by impregnation of nano silica sol. *Polymers* 2020;12:1632. DOI PubMed PMC
32. Han M, Yu Jie. Subnanoscopically and homogeneously dispersed SiO_x/C composite spheres for high-performance lithium ion battery anodes. *J Power Sources* 2019;414:435-43. DOI
33. Lu B, Ma B, Deng X, et al. Cornlike ordered mesoporous silicon particles modified by nitrogen-doped carbon layer for the application of Li-ion battery. *ACS Appl Mater Interfaces* 2017;9:32829-39. DOI PubMed
34. Kuang S, Xu D, Chen W, et al. In situ construction of bamboo charcoal derived SiO_x embedded in hierarchical porous carbon framework as stable anode material for superior lithium storage. *Appl Surf Sci* 2020;521:146497. DOI
35. Mu T, Zuo P, Lou S, et al. A three-dimensional silicon/nitrogen-doped graphitized carbon composite as high-performance anode material for lithium ion batteries. *J Alloy Compd* 2019;777:190-7. DOI

36. Xue H, Wu Y, Zou Y, et al. Unraveling metal oxide role in exfoliating graphite: new strategy to construct high-performance graphene-modified SiO*x*-based anode for lithium-ion batteries. *Adv Funct Mater* 2020;30:1910657. DOI
37. Meng Q, Li G, Yue J, et al. High-performance lithiated SiO*x* anode obtained by a controllable and efficient prelithiation strategy. *ACS Appl Mater Interfaces* 2019;11:32062-8. DOI
38. Guo X, Xu H, Li W, et al. Embedding atomically dispersed iron sites in nitrogen-doped carbon frameworks-wrapped silicon suboxide for superior lithium storage. *Adv Sci* 2023;10:e2206084. DOI PubMed PMC
39. Zhuang D, Zhang Y, He R, et al. Converting bulk $MoSi_2$ alloy to a SiO*x* based anode material through controlled oxidation induced sublimation. *Mater Chem Front* 2023;7:3650-6. DOI
40. Jin M, Zhou H, Sun G, Zhao J, Li J. Sulfur-induced porous carbon nanofibers composite SiO as bifunctional anode for high-performance Li-ion storage. *J Mater Sci* 2022;57:5954-63. DOI
41. Xiao Y, Mao Y, Li T, Hao X, Wang W. Facile synthesis of a SiO*x*graphite composite toward practically accessible high-energy-density lithium-ion battery anodes. *ACS Appl Mater Interfaces* 2023;15:45938-48. DOI
42. Xu Y, Li Y, Qian Y, Sun S, Lin N, Qian Y. Deficient TiO_{2-x} coated porous SiO anodes for high-rate lithium-ion batteries. *Inorg Chem Front* 2023;10:1176-86. DOI
43. Ma J, Song C, Chen S, Xu Y, Du H. Drop-casting preparation of a binder-free SiO_x anode with micron-sized SiO_x particles for high-performance lithium-ion batteries. *J Alloy Compd* 2022;918:165682. DOI
44. Wu Y, Nie P, Wu L, Dou H, Zhang X. 2D MXene/SnS_2 composites as high-performance anodes for sodium ion batteries. *Chem Eng J* 2018;334:932-8. DOI
45. Zhou J, Jiang S, Li Y, et al. Chemical fixation of CO_2 on activated Si: producing graphitic carbon-stabilized Si particles for Li-storage. *Energy Storage Mater* 2020;31:36-43. DOI